Monthly Notices
of the
ROYAL ASTRONOMICAL SOCIETY

Mon. Not. R. Astron. Soc. **412,** 1070–1080 (2011) doi:10.1111/j.1365-2966.2010.17960.x

Supernova dust for the extinction law in a young infrared galaxy at $z \sim 1$

K. Kawara,[1⋆] H. Hirashita,[2] T. Nozawa,[3] T. Kozasa,[4] S. Oyabu,[5] Y. Matsuoka,[5] T. Shimizu,[1] H. Sameshima[1] and N. Ienaka[1]

[1]*Institute of Astronomy, the University of Tokyo, Osawa 2-21-1, Mitaka, Tokyo 181-0015, Japan*
[2]*Institute of Astronomy and Astrophysics, Academia Sinica, PO Box 23-141, Taipei 10617, Taiwan*
[3]*Institute for the Physics and Mathematics of the Universe, the University of Tokyo, 5-1-5 Kashiwanoha, Kashiwa 277-8568, Japan*
[4]*Department of Cosmosciences, Hokkaido University, Sapporo 060-0810, Japan*
[5]*Graduate School of Science, Nagoya University, Furo-cho, Chikusa-ku, Nagoya 464-8602, Japan*

Accepted 2010 November 2. Received 2010 November 1; in original form 2010 March 1

ABSTRACT

We apply the supernova (SN) extinction curves to reproduce the observed properties of SST J1604+4304 which is a young infrared (IR) galaxy at $z \sim 1$. The SN extinction curves used in this work were obtained from models of unmixed ejecta of Type II supernovae for the Salpeter initial mass function with a mass range from 8 to 30 $M_\odot$ or 8 to 40 $M_\odot$. The effect of dust distributions on the attenuation of starlight is investigated by performing the χ^2 fitting method against various dust distributions. These are the commonly used uniform dust screen, the clumpy dust screen and the internal dust geometry. We add to these geometries three scattering properties, namely, no scattering, isotropic scattering and forward-only scattering. Judging from the χ^2 values, we find that the uniform screen models with any scattering property provide good approximations to the real dust geometry. Internal dust is inefficient to attenuate starlight and thus cannot be the dominant source of the extinction. We show that the SN extinction curves reproduce the data of SST J1604+4304 comparable to or better than the Calzetti extinction curve. The Milky Way extinction curve is not in satisfactory agreement with the data unless several dusty clumps are in the line of sight. This trend may be explained by the abundance of SN-origin dust in these galaxies; SN dust is the most abundant in the young IR galaxy at $z \sim 1$, abundant in local starbursts and less abundant in the Galaxy. If dust in SST J1604+4304 is dominated by SN dust, the dust production rate is $\sim$0.1 $M_\odot$ per SN.

Key words: supernovae: general – dust, extinction – galaxies: evolution – galaxies: ISM – galaxies: starburst – infrared: galaxies.

1 INTRODUCTION

Dust is a minor constituent in the Universe , but it plays crucial roles for evolution of various objects; for example, it cools gas clouds by radiating far-infrared (far-IR) emission, and acts as a catalyzer to form molecules. Corrections for dust extinction have significant cosmological consequences for determining the Hubble constant, the cosmological model and the epoch of galaxy formation.

It is generally accepted that the atmospheres of asymptotic giant branch (AGB) stars are one of the main sources of interstellar dust in the Milky Way (MW). However, AGB stars are too old to account for the presence of dust at $z > 6$ (but see Valiante et al. 2009), and supernovae (SNe) have been recognized as a candidate of the major source of dust in the early stage of galaxy evolution.

Stars with masses 8–40 $M_\odot$ end up their life as Type II supernovae (SNe II)[1] in $\leq$40 Myr since their formation (Heger et al. 2003). The formation of dust in SN ejecta was first witnessed in SN 1987A, motivating Kozasa, Hasegawa & Nomoto (1989) and Kozasa, Hasegawa & Nomoto (1991) to predict the condensed dust composition and size. Systematic studies of dust formation in SN ejecta have been proceeded to explore the role of dust in the formation and evolution of stars and galaxies in the early universe (Todini & Ferrara 2001; Nozawa et al. 2003; Schneider, Ferrara & Savaterra 2004): the composition of synthesized dust reflects the elemental composition in the formation site which is affected by the type and degree of mixing and the degree of formation efficiency of CO

[1] In this paper, we simply use the term SNe II for core-collapsed SNe whose progenitors are massive stars. We also call the dust produced by SNe II 'SN dust', and the extinction curve synthesized for the SN dust 'SN extinction curve'.

⋆E-mail: kkawara@ioa.s.u-tokyo.ac.jp

molecule, and the size of dust is controlled by the time evolution of gas density and temperature depending on the type of SNe (Nozawa et al. 2008, 2010).

Apart from the differences in the SN models and the underlying assumptions employed for dust formation calculations, the predicted dust mass formed in the ejecta reaches 0.1 to 1 $M_\odot$ per SN II, which is sufficient enough to explain a vast amount of dust of $>10^8$ $M_\odot$ discovered in host galaxies of high-redshifted quasars [quasi-stellar objects (QSOs)] at $z > 5$ (e.g. Morgan & Edmunds 2003; Maiolino et al. 2006; Dwek., Galliano & Jones 2007). However, the mass and composition of dust formed in the ejecta have been still controversial; the observations of nearby SNe have claimed dust mass formed in the ejecta to be less than 10^{-3} $M_\odot$ (see Kozasa et al. 2009 for a review), while the infrared and submillimetre observations of Galactic supernova remnants (SNRs) have suggested the presence of dust reaching 0.02 to 1 $M_\odot$ (Dunne et al. 2003, 2009; Rho et al. 2008; Gomez et al. 2009; Nozawa et al. 2010; Temim et al. 2010). Although no information has been available on the composition of dust formed in the ejecta except for SN 2004et (Kotak et al. 2009), the spectral mapping observation covering the entire of Cas A SNR with the *Spitzer Space Telescope* have revealed the presence of a variety of dust species whose composition is closely associated with the gas emission-line characteristic of nucleosynthetic layer in the progenitor (Rho et al. 2008).

The amount, composition and size of dust supplied from SNe to the interstellar medium (ISM) are not always the same as those condensed in the ejecta due to the processing in a hot plasma produced by the reverse and forward shocks during the journey to the ISM (Bianchi & Schneider 2007; Nozawa et al. 2007) as well as in the hot/warm region of ISM (Jones et al. 1994; Jones, Tielens & Hollenbach 1996; Nozawa, Kozasa & Habe 2006; Hirashita et al. 2010). Nevertheless, Maiolino et al. (2004) found that the extinction curve of SDSS J1048+4647, a broad absorption line (BAL) QSO at $z = 6.2$ is different from those of nearby galaxies, and is in excellent agreement with the extinction curve obtained from SN dust models by Todini & Ferrara (2001) considering the uniformly mixed elemental composition in the ejecta (see also Gallerani et al. 2010). Synthesizing dust extinction curves for various SN dust models by Nozawa et al. (2003), Hirashita et al. (2005) have shown that the extinction curve observed in this BAL QSO can be reasonably reproduced by the dust produced in SNe II without any mixing in the ejecta. Furthermore, the extinction curve derived from the analysis of the afterglow of γ-ray burst GRB 050904 at $z = 6.3$ have suggested that SNe are the dominant source of dust in the host galaxy (Stratta et al. 2007), although Zafar et al. (2010) have claimed no evidence of dust extinction in the afterglow. However, the observed extinction curve in the local environments may provide less constraint on the SN dust model as well as the role of SNe on the evolution of galaxies.

Young galaxies, in which no AGB stars evolved off the main sequence, are obvious targets to study the properties of SN dust, for example, extinction curves that determine the relation between changes in colour and total absorption. However, it is generally difficult to infer the amount of the dust obscuration, because different geometries of the dust spatial distribution result in different observed colours for the same amount of dust and the same intrinsic spectrum of the underlying stellar population (e.g. Giavalisco 2002). In fact, some studies of H I recombination lines in starburst and dusty Seyfert galaxies suggest that the extinction observed in the near-IR is generally greater than that observed by using the optical lines (Kawara, Nishida & Phillips 1989; Puxley & Brand 1994).

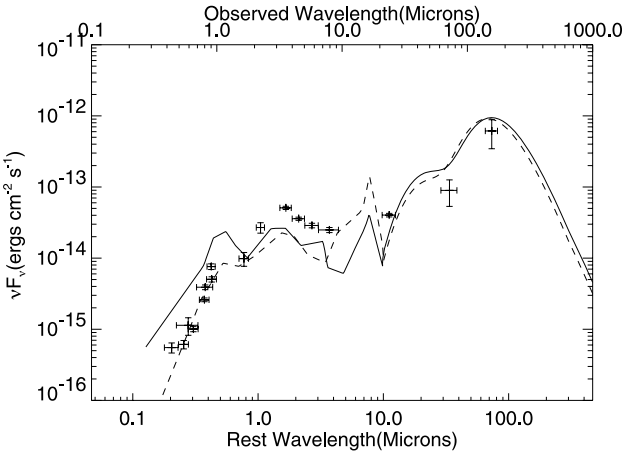

Figure 1. UV to far-IR SED for SST J1604+4304 compared with those of starburst-dominated ULIRGs, Arp 220(solid: local ULIRG), MIPS J142824.0+352619(dash: $z = 1.3$ hyperluminous IR galaxy). Arp 220 data come from Carico et al. (1990), Rigopoulou, Lawrence & Rowan-Robinson (1996) and Klaas et al. (1997), and MIPS J142824.0+352619 from Desai et al. (2006) and Borys et al. (2006).

Calzetti, Kinney & Storchi-Bergmann (1994) have shown that the extinction laws in the MW and Large Magellanic Cloud cannot account for the ultraviolet (UV) to optical spectra of UV-bright starburst galaxies in the local Universe in a satisfactory way. They empirically derived the extinction law for these galaxies. Their extinction law is characterized by an overall slope which is more grey or flatter than the MW extinction law's slope and by the absence of the 2175 Å dust feature. In starburst galaxies, numerous SN II explosions occur and SN-condensed dust would be injected into the ISM. Thus, newly formed SN dust would produce a great impact on the extinction law in local starbursts.

In this paper, we apply synthetic extinction curves on the unmixed ejecta models of SNe II by Hirashita et al. (2005) to the broad-band spectral energy distribution (SED) of a young ultraluminous infrared galaxy (ULIRG) SST J1604+4304 at $z \sim 1$. Comparing with the MW and Calzetti (2001) extinction laws, we show that the SN extinction curves fit better to the observations. We adopt $H_0 = 70\,\mathrm{km\,s^{-1}\,Mpc^{-1}}$, $\Omega_\mathrm{m} = 0.3$ and $\Omega_\Lambda = 1 - \Omega_\mathrm{m}$ throughout this paper.

2 DATA

Synthetic spectra of stellar populations reddened by dust are modelled to reproduce the data of SST J1604+4304. This is a young IR galaxy at $z = 1.135$ with the characteristic of ULIRGs. The multiwavelength data from the X-ray to radio are compiled in Kawara et al. (2010). There are no supportive evidence for active galactic nucleus (AGN) activities in this galaxy, although the data are not deep enough to rule out the presence of an AGN.

Fig. 1 illustrates the broad-band SED from the UV to far-IR[2] along with representative SED templates of starburst-dominated ULIRGs, namely, Arp 220 (local ULIRG) and MIPS J142824.0+352619 (hyperluminous IR galaxy at $z = 1.3$). The broad-band SED and stellar absorption lines, such as Ca II and H I lines, as well as the [O II]λ3727 line suggest that young stellar populations dominate the

[2] The data are taken from table 1 in Kawara et al. (2010) and the correction for the gravitational amplification is applied.

optical luminosity in this galaxy. The Ca II index, defined by Kawara et al. (2010), is $D(\mathrm{Ca\,II}) = 0.03 \pm 0.11$ and the equivalent [O II] width is EW([O II]) $= 31.1 \pm 4.3$ Å in the rest frame which corresponds to the observed [O II] line flux[3] of $1.9 \pm 0.3 \times 10^{-17}$ erg cm^{-2} s^{-1}.

Kawara et al. (2010) estimated the reddening to be $E(B-V) \sim 0.8$ when the Calzetti extinction law is applied. The 8–1000 μm bolometric luminosity inferred from the three *Spitzer* MIPS bands at the 24, 70 and 160 μm is $L_{\rm ir} = 1.78 \pm 0.63 \times 10^{12}\,\mathrm{L}_{\odot}$, corresponding to the flux $F_{\rm ir} = 1.00 \pm 0.35 \times 10^{-12}$ erg cm^{-2} s^{-1}. These values are intrinsic to the galaxy after correcting for a gravitational amplification of 1.17 by the foreground galaxy cluster CL 1604+4304 at $z = 0.9$. The bolometric luminosity agrees with the extinction-corrected stellar luminosity, suggesting SST J1604+4304 can be characterized by models of pure star formation with no AGN emission. The dust mass inferred from the far-IR data is $\sim 2 \times 10^8\,\mathrm{M}_{\odot}$, sufficient to form a shell surrounding the galaxy and produce the observed extinction.

The SED data at 13 photometric bands from B to 5.8 μm are used for the following analysis; the longest *Spitzer* IRAC 8.0-μm band is not used, because the dust emission may be greater than the starlight in this band corresponding to 3.7 μm in the rest frame.

3 EXTINCTION

3.1 Geometry of dust distribution

The attenuation of starlight produced by dust in front of an extended source not only depends on the properties of dust grains, such as cross-sections, albedo and amount, but also depends on the geometry of spatial distribution of dust. It is known that the apparent optical depth is lower than the optical depth averaged over the source area when starlight is attenuated by a thick, clumpy dust layer or dust is internal to the extended source. We consider the following geometries of dust distribution. For full details, the reader may refer to Code (1973), Natta & Panagia (1984) and Calzetti et al. (1994).

Internal dust. In the case that absorbers (dust grains) and emitters (stars) are uniformly distributed, the apparent extinction is given by

$$f_\nu = \epsilon_{\rm in} f_\nu^0 \qquad \text{with } \epsilon_{\rm in} = \mathrm{e}^{-\tau_{\rm ap}}, \tag{1}$$

$$\tau_{\rm ap} = -\ln[(1-\mathrm{e}^{-\tau_{\rm eff}})/\tau_{\rm eff}], \tag{2}$$

$$\tau_{\rm eff} = (1-\gamma)\tau_{\rm ext} \qquad \text{for } g = 1, \tag{3}$$

$$\tau_{\rm eff} = (1-\gamma)^{0.75}\tau_{\rm ext} \qquad \text{for } g = 0, \tag{4}$$

where $\tau_{\rm ap}$ is the apparent optical depth of the internal dust, $\tau_{\rm eff}$ the effective absorption optical depth, $\tau_{\rm ext}$ the sum of the optical depth for absorption and scattering, γ the albedo, f_ν^0 is the unobscured, intrinsic flux density and f_ν is the reddened, observed flux density. $g \equiv \langle\cos(\theta)\rangle$ is the scattering asymmetry factor, where $g = 1$ for the forward-only scattering and $g = 0$ for the isotropic scattering. Sometimes $\tau_{\rm eff} = (1-\gamma)^{0.5}\tau_{\rm ext}$ is used for the isotropic scattering (i.e. Natta & Panagia 1984; Calzetti et al. 1994). However, $\tau_{\rm eff} = (1-\gamma)^{0.75}\tau_{\rm ext}$ approximates better to the solution by the two-stream approximation for the geometry with a uniform distribution of the absorbers and the emitters. For the full details, refer to Fig. A1 in Appendix A.

[3] The [O II] line flux published in Kawara et al. (2010) is incorrect.

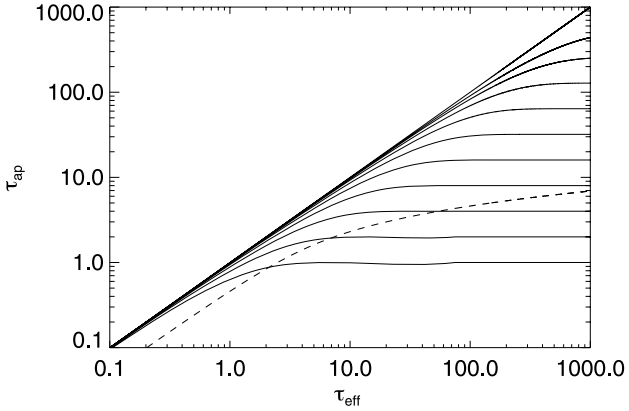

Figure 2. The apparent optical depth $\tau_{\rm ap}$ is shown as a function of the effective optical depth $\tau_{\rm eff}$. The solid lines represent dust screen geometries for $N = [1, 2, 4, 8, 16, 32, 64, 128, 256, 512, \infty]$ from bottom to top. The dashed line represents an internal dust geometry.

Dust screen. In this geometry, the absorbers are physically separated and located in a screen in front of the emitters. We adopt an analytic expression derived by Natta & Panagia (1984) for a system of clumps distributed according to Poisson statistics:

$$f_\nu = \epsilon_{\rm sc} f_\nu^0 \qquad \text{with } \epsilon_{\rm sc} = \mathrm{e}^{-\tau_{\rm ap}}, \tag{5}$$

$$\tau_{\rm ap} = N(1-\mathrm{e}^{-\tau_{\rm eff}/N}), \tag{6}$$

where N is the average number of clumps along the line of sight, and all clumps are assumed to have one and the same effective optical depth $\tau_{\rm eff}/N$. For $N \to \infty$, $\tau_{\rm ap} \to \tau_{\rm eff}$, corresponding to the uniform dust screen. For the dust screen which is physically distant from the system of stars, the effect of the dust is to remove photons from the line of sight through absorption and scattering. On the other hand, for the dust screen which is located close to the system of stars, the scattered photons can get in the line of sight. Thus, $\tau_{\rm eff}$ is given as

$$\tau_{\rm eff} = \tau_{\rm ext} \qquad \text{for no scattering,} \tag{7}$$

$$\tau_{\rm eff} = (1-\gamma)\tau_{\rm ext} \qquad \text{for scattering with } g = 1, \tag{8}$$

$$\tau_{\rm eff} = (1-\gamma)^{0.5}\tau_{\rm ext} \qquad \text{for scattering with } g = 0. \tag{9}$$

Again, $g = 1$ is for the forward-only scattering, and $g = 0$ for the isotropic scattering.

Composite geometry. It is quite likely that dust grains distribute within the system of stars as internal dust and in the screen in front of the system. We approximate this case as

$$f_\nu = \epsilon_{\rm sc}\epsilon_{\rm in} f_\nu^0. \tag{10}$$

Fig. 2 shows the apparent optical depth $\tau_{\rm ap}$ as a function of $\tau_{\rm eff}$. It is apparent that the growth of $\tau_{\rm ap}$ turns over at a smaller value of $\tau_{\rm eff}$ in the dust screen with a smaller value of N. As shown in this figure, the extinction by dust in the screen with a small N or by internal dust strongly depends on the geometry and tends to produce a grey extinction, and dust in a uniform screen produces the most effective extinction.

3.2 Extinction curves

We examine two extinction curves synthesized in ejecta of SNe II: the empirical extinction curve derived by Calzetti (2001), and the MW extinction curve given by Draine (2003). Fig. 3 plots these extinction curves as a function of wavelengths, showing that the

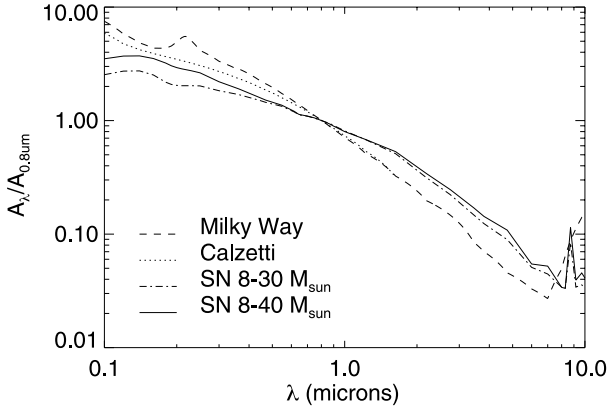

Figure 3. Synthetic SN extinction curve compared with those for the MW (Draine 2003) and local starbursts (Calzetti 2001). The curves are normalized to the extinction (absorption + scattering) in magnitude at 0.8 μm. Note that a spike on the SN curve is produced by crystal SiO_2 at 8.7 μm.

SN extinction curves are more grey or flatter than the Calzetti and MW extinction curves from 0.1 to 1 μm.

The MW extinction curve exhibits a pronounced feature at 2175 Å. This feature is absent in the typical extinction curves of the Small Magellanic Clouds (SMC). The dust in local starbursts and Lyman break galaxies exhibits the properties of the SMC-like dust properties, while Noll et al. (2009) claimed that about 30 per cent of the spectra of actively star-forming, intermediate-mass galaxies at $1 < z < 2.5$ exhibit broad absorption features at ∼2175 Å. To check the effect of the feature on the extinction law in SST J1604+4303, in addition to the MW extinction curve by Draine (2003), we will examine the pseudo-MW extinction curve which is made by removing the 2175-Å feature from the MW extinction curve.

The Calzetti (2001) extinction curve was derived by analysing local starbursts and blue compact dwarf galaxies (Calzetti et al. 1994), and is widely used to, for example, derive photometric redshifts of high-redshift galaxies. Calzetti (2001) gives the extinction curve in a narrow range from 0.12 to 2.2 μm. To analyse multi-wavelength data of high-redshift objects from the UV to IR such as given in Fig. 1, the extinction curve should be extended to longward of 2.2 μm. The functional form given by Calzetti (2001) cannot be used to extend the extinction curve, because the extinction value sharply drops beyond 2.2 μm. The Calzetti extinction curve is almost identical to the Draine (2003)'s MW curve from 0.6 to 1.6 μm. We thus extend the Calzetti curve to longer wavelengths by adopting the MW extinction curve for wavelengths ≥1.6 μm. In addition, because Calzetti (2001) does not provide the albedo, we adopt the albedo given in Draine (2003) with removing the dip in the albedo which is attributed to the familiar 2175-Å feature. This curve is called the Calzetti extinction curve in this paper. It is quite likely that the Calzetti extinction curve reflects the dust composition from the two origins, namely dust condensed in expanding atmospheres of AGB stars and ejecta of SNe II, because in local starburst galaxies low-mass stars have already evolved off the main sequence and reached to the dust-forming stages. Because the Calzetti curve was empirically obtained by assuming a geometry of uniform foreground screens (i.e. $f_\nu = \mathrm{e}^{-\tau} f_\nu^0$), we apply this curve in this form only.

The two SN extinction curves are compared with the MW and Calzetti extinction curves. The SN extinction curves were synthesized in unmixed ejecta of SNe II by Hirashita et al. (2005), based on the dust production models by Nozawa et al. (2003). Nozawa et al. (2003) have investigated the dust condensation in SNe II with various progenitor masses, taking into account the time evolution of gas temperatures in the ejecta by solving the radiative transfer equation with energy deposition of radioactive elements. The two extreme cases are considered for the elemental composition in the He core: the unmixed case and the uniformly mixed case. The formation of all possible condensations is calculated simultaneously by applying a theory of non-steady state nucleation and grain growth under the assumption of complete formation of CO and SiO molecules. Various dust species condense according to the elemental composition at the formation site in the unmixed ejecta; carbon in the inner C-rich He layer, Al_2O_3, Mg silicates (Mg_2SiO_4 and $MgSiO_3$) in the O-rich layer, MgO in the outer O-rich layer, SiO_2 in the inner O-rich layer, Si and FeS in the Si–S layer and FeS and Fe in the inner most Fe–S layer. In the mixed ejecta, only oxide grains such as Al_2O_3, Mg silicates, SiO_2 and Fe_3O_4 condense because the elemental composition assuming complete formation of CO is oxygen rich in the entire He core. In the unmixed cases, C and Si dust species dominate the dust mass in the low-mass progenitor (Nozawa et al. 2003), and Mg_2SiO_4 is getting dominant with increasing progenitor mass, while in the mixed ejecta SiO_2 and Mg_2SiO_4 dust dominate the dust mass.

Combining the optical constants in the literature with the grain species and size distribution of SN-condensed dust derived by Nozawa et al. (2003), and using the Mie theory, Hirashita et al. (2005) have calculated absorption and scattering cross-sections of homogeneous spherical grains with various sizes condensed in mixed and unmixed ejecta. It should be pointed out here that in the unmixed ejecta C and Si dust grains with radius $a \geq 0.1\,\mu\mathrm{m}$ are significantly abundant in the low-mass progenitors than in the high-mass progenitors. This results in the different behaviour of the extinction curves: the extinction curve in UV region tends to be flatter in the unmixed cases than in the mixed cases (Hirashita et al. 2005). The details for the adopted quantities are described in Hirashita et al. (2005). The extinction curves in unmixed ejecta of SNe II reasonably reproduce the extinction law of the $z = 6.2$ BAL QSO found by Maiolino et al. (2004). In this paper, we use the two extinction curves of unmixed SNe II for the Salpeter (1955) initial mass function (IMF); one has a mass range of progenitors from 8 to $30\,\mathrm{M}_\odot$, and the other from 8 to $40\,\mathrm{M}_\odot$. These were obtained by interpolating or extrapolating extinction curves that Hirashita et al. (2005) calculated for unmixed SNe II with progenitor masses of 13, 20, 25 and $30\,\mathrm{M}_\odot$.[4]

4 SYNTHETIC SPECTRA OF STELLAR POPULATIONS

The evolutionary synthesis codes by Bruzual & Charlot (2003) are used to generate synthetic spectra of evolutionary stellar population models. We adopt the Salpeter (1955) IMF with the lower and upper mass cut-offs of 0.1 and $100\,\mathrm{M}_\odot$, respectively. It is noted that the weight of massive stars is greater in the Chabrier (2003) IMF than in the Salpeter IMF, resulting in a mass to luminosity ratio roughly 1.6 times heavier in the Salpeter IMF. The star formation histories are exponentially declining models with the star formation rate (SFR) $\propto t_{\mathrm{sfr}}^{-1} \exp(-t/t_{\mathrm{sfr}})$, where t_{sfr} is the e-folding time-scale and t is the

[4] In Hirashita et al. (2005), the slope of extinction curve for 25 and $30\,\mathrm{M}_\odot$ progenitors was overestimated because of the error in the calculation processes. We have replaced the results with correct ones. Nevertheless, the conclusions in Hirashita et al. (2005) are not altered by this change.

age, i.e. the time after the onset of the first star formation. Although Kawara et al. (2010) used the instantaneous burst models, such models are not appropriate to reproduce simultaneously the strong [O II]λ3727 emission line from H II regions ionized by young, hot stars and the observed SED. The synthetic spectra are generated in a parameter range of $t = 3 \times 10^5$ to 8×10^9 yr in a step of 0.2 dex and $t_{\rm sfr} = 10^6$ to 1.6×10^{10} yr in a step of 0.3 dex. For the shortest $t_{\rm sfr}$, the star formation history is near an instantaneous burst, while for the longest $t_{\rm sfr}$, the star formation rate is almost constant over the cosmic time. The metallicity of the synthetic spectra has a range of $Z = 0.005$–$2.5\,{\rm Z}_\odot$ (i.e. six points at 0.005, 0.02, 0.2, 0.4, 1.0 and $2.5\,{\rm Z}_\odot$).

The extinction models discussed in Section 3 are then applied to the synthetic spectra generated in the above procedure, yielding template spectra which are used for the subsequent χ^2 fitting. In the initial run, the extinction measured at 0.3 μm has a range of $\tau_{\rm ext}(0.3\,\mu{\rm m}) = 0$–10 in a step of 0.1. In case that the initial range is too narrow to have the minimum χ^2 for a certain model, the range and the step are widen by a factor of 3 to search for the minimum χ^2, and so on.

5 χ^2 TEMPLATE-FITTING METHOD

We search for the best set of parameters for SST J1604+4304 by using a χ^2 template-fitting method as defined below:

$$\chi^2 = \chi^2_{\rm SED} + \chi^2_{\rm [O\,II]} + \chi^2_{\rm Ca\,II} + \chi^2_{\rm fir}, \tag{11}$$

where the degree of freedom is $\nu = 12$. In what follows, we define the terms in equation (11):

$$\chi^2_{\rm SED} = \sum_{\rm filters} (F_{\rm obs} - bF_{\rm template})^2/\sigma^2_{\rm SED}, \tag{12}$$

where b is the parameter determined by fitting the template flux density $F_{\rm template}$ to the observed $F_{\rm obs}$. $F_{\rm obs}$ are the photometric data measured in 13 broad-band filters from B to 5.8 μm. The *Spitzer* IRAC 8.0 μm is not used, because dust emission may be significant in this band corresponding to 3.7 μm in the rest frame. It is noted that 5 per cent of the flux was added in the quadratic form to the photometric error $\sigma_{\rm ph}$, i.e. $\sigma^2_{\rm SED} = \sigma^2_{\rm ph} + (0.05F_{\rm obs})^2$. This is necessary to avoid too small and non-realistic photometric error.

The strong [O II]λ3727 line requires the presence of OB stars. We thus include $\chi^2_{\rm [O\,II]}$ in the χ^2 template-fitting method. $\chi^2_{\rm [O\,II]}$ is defined as

$$\chi^2_{\rm [O\,II]} = \left({\rm EW}^{\rm [O\,II]}_{\rm obs} - {\rm EW}^{\rm [O\,II]}_{\rm template}\right)^2/\sigma^2_{\rm [O\,II]}, \tag{13}$$

where ${\rm EW}^{\rm [O\,II]}_{\rm obs} = 31.1 \pm 4.3$ Å. To derive ${\rm EW}^{\rm [O\,II]}_{\rm template}$, we first obtain the Hα luminosity by counting ionizing photons in the synthesized spectra. We then adopt the [O II] and Hα calibration performed by Kewley, Geller & Jansen (2004). For the metallicity scaling of [O II]/Hα, we use their theoretical curves for $q = 3 \times 10^7\,{\rm cm\,s^{-1}}$ with an additional condition that [O II]/Hα should not be less than 0.1. This additional condition is applied to avoid a negative or unrealistic value of [O II]/Hα outside of the calibrated range of metallicity. The calibrated [O II]/Hα has a peak value of 1.6 at $Z = 0.4\,{\rm Z}_\odot$ and drops to a value of 0.1 at $Z = 0.14\,{\rm Z}_\odot$ or $Z = 2.44\,{\rm Z}_\odot$. Because Kewley et al. (2004) estimated the uncertainty to be ∼ 30 per cent, we add this uncertainty to the observational error as $\sigma^2_{\rm SED} = \sigma^2_{\rm [O\,II]SED} + (0.3\,{\rm EW}^{\rm [O\,II]}_{\rm template})^2$.

As discussed in Kawara et al. (2010), the D(Ca II) index, which is the ratio of the Ca II to H I absorption lines in equivalent width, is useful to measure the age of the relatively old stellar populations. $\chi^2_{\rm Ca\,II}$ is defined as

$$\chi^2_{\rm Ca\,II} = (D({\rm Ca\,II})_{\rm obs} - D({\rm Ca\,II})_{\rm template})^2/\sigma^2_{D({\rm Ca\,II})}, \tag{14}$$

where $\sigma_{D({\rm Ca\,II})}$ is the observational error.

The luminosity absorbed by dust should mostly be re-emitted in the far-IR. If the energy source of the galaxy is dominated by star formation, the absorbed luminosity should match with the far-IR luminosity. We include this effect as follows:

$$\chi^2_{\rm fir} = (F_{\rm ir} - F_{\rm absorbed})^2/\sigma^2_{\rm ir}, \tag{15}$$

where $F_{\rm ir}$, $F_{\rm absorbed}$ and $\sigma_{\rm ir}$ are the observed flux in 8–1000 μm, the absorbed flux in the UV to near-IR and the observed error of $F_{\rm ir}$, respectively. It is noted that $F_{\rm absorbed}$ is calculated for a given b which is determined by $\partial\chi^2_{\rm SED}/\partial b = 0$.

6 RESULTS

First of all, the Calzetti extinction models, which have a uniform foreground screen, yield the best-fitting model having the reduced χ square $\chi^2_\nu = 5.1$ with $\chi^2_{\rm [O\,II]} = 0.0$, $\chi^2_{\rm Ca\,II} = 0.3$ and $\chi^2_{\rm fir} = 0.9$. This model has a parameter set of the optical depth $\tau_{\rm ext}(0.3\,\mu{\rm m}) = 5.3$, the age $t = 2.0 \times 10^8$ yr with the star formation time-scale of $t_{\rm sfr} = 6.3 \times 10^7$ yr and the metallicity in stellar atmosphere $Z = 1\,{\rm Z}_\odot$, EW([O II]) = 29 Å, D(Ca II) = 0.09 and $F_{\rm absorbed} = 6.6 \times 10^{-13}\,{\rm erg\,cm^{-2}\,s^{-1}}$. This is our reference to which the goodness of our other models will be judged.

The left-hand panels of Fig. 4 plot χ^2_ν as a function of $\tau_{\rm in}/(\tau_{\rm in} + \tau_{\rm sc})$ for the uniform foreground screen mixed with internal dust. $\tau_{\rm in}$ and $\tau_{\rm sc}$ are $\tau_{\rm ext}$ for internal dust and screen dust, respectively. For the pure internal dust geometry, $\tau_{\rm in}/(\tau_{\rm in} + \tau_{\rm sc}) = 1$, while the pure foreground screen geometry, $\tau_{\rm in}/(\tau_{\rm in} + \tau_{\rm sc}) = 0$. The scattering properties are assumed to be the no scattering, the isotropic scattering ($g = 0$) or the forward-only scattering ($g = 1$). In case of no scattering, forward scattering is assumed for internal dust.

The pseudo-MW extinction curve, which is made by removing the 2175-Å feature from the MW extinction curve, has a smaller χ^2_ν than the MW extinction curve, suggesting the 2175-Å feature is very weak or unrecognizable in SST J1604+4304. Because of the large χ^2_ν values[5] relative to the Calzetti and SN extinction curves, the MW extinction curve is unlikely regardless of the presence of the 2175-Å feature. The pure internal dust geometry can be ruled out regardless of the choice of extinction curves. Another difficulty of the pure internal geometry is that too much dust is required to reproduce the observed SED (i.e. $\tau_{\rm ext} = 70$–200). The estimated dust mass is far greater than that observed by a factor of 10 or even more. The general trend is that χ^2_ν becomes smaller as $\tau_{\rm in}/(\tau_{\rm in} + \tau_{\rm sc})$ approaching to zero, indicating that the extinction due to internal dust is a small fraction of the total extinction as already found in highly reddened H II regions (i.e. Natta & Panagia 1984). The two SN extinction curves have χ^2_ν less than that of the Calzetti extinction curve (i.e. $\chi^2_\nu = 5.1$) for a typical range of $\tau_{\rm in}/(\tau_{\rm in} + \tau_{\rm sc}) = 0.0$–0.7.

The middle and right-hand panels of Fig. 4 plot χ^2_ν as a function of the number of clumps along the line of sight for the clumpy foreground screen; pure clumpy foreground screens (i.e. $\tau_{\rm in}/(\tau_{\rm in} + \tau_{\rm sc}) = 0$) are shown in the middle panels and foreground screens with internal dust having $\tau_{\rm in}/(\tau_{\rm in} + \tau_{\rm sc}) = 0.4$ in the right-hand

[5] The approximate values of the increment of χ^2_ν are 1.14, 1.75 and 2.36 for 68 per cent(1σ), 95 per cent (2σ) and 99.6 per cent (3σ) confidence where the degree of freedom is $\nu = 12$ (Avni 1976).

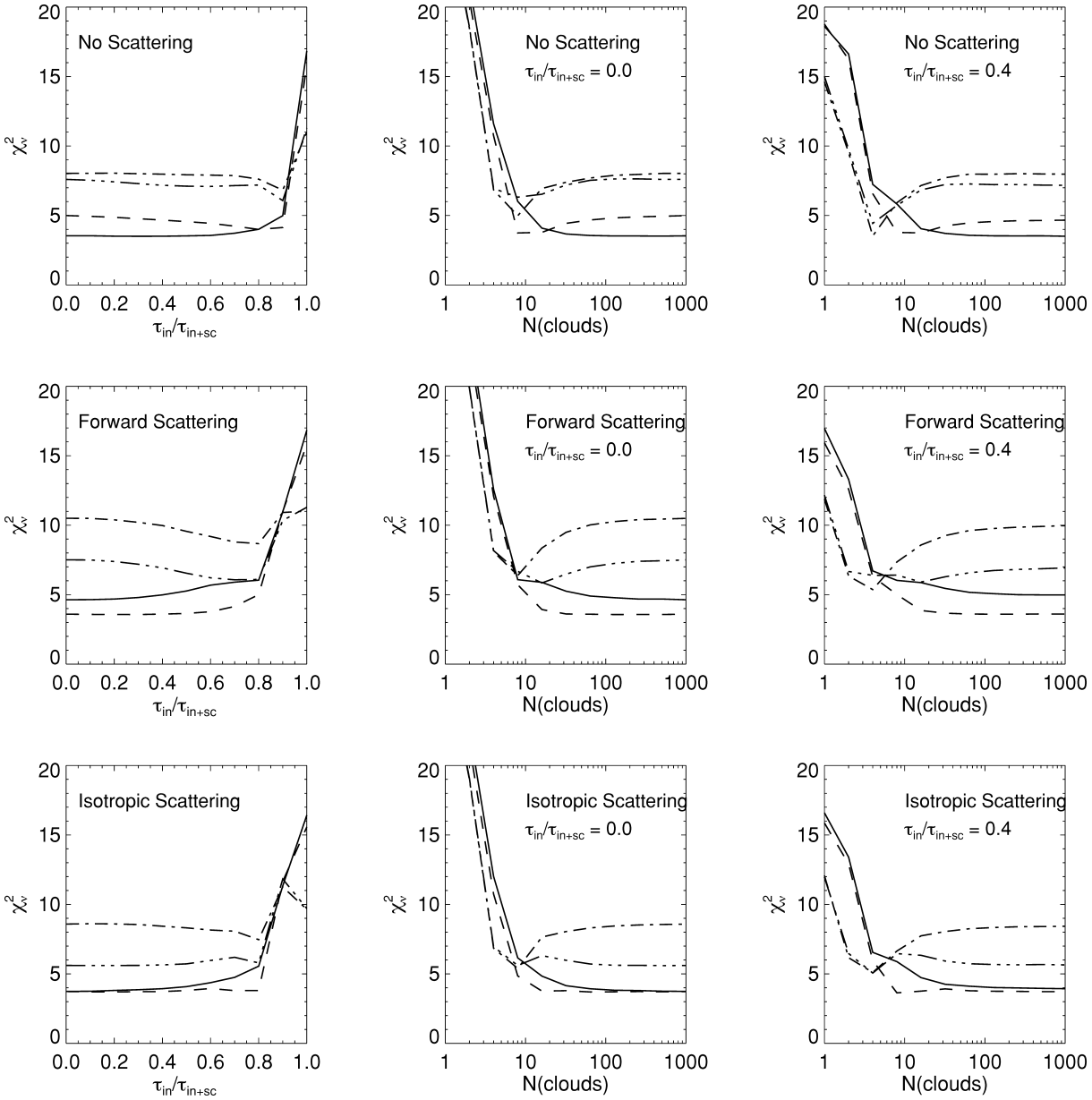

Figure 4. The left-hand panels show χ^2_ν ($\nu = 12$) as a function of $\tau_{\rm in}/(\tau_{\rm in} + \tau_{\rm sc})$ for no scattering (top), forward scattering (middle) and isotropic scattering (bottom), where $\tau_{\rm in}$ is the optical depth for internal dust and $\tau_{\rm sc}$ for screen dust. The uniform screen is assumed. In case of no scattering, forward scattering is assumed for internal dust. Solid lines represent SN dust with 8–30 $M_\odot$, dash lines SN dust with 8–40 $M_\odot$, dash–dot lines MW dust and dash–dot–dot lines pseudo-MW dust without the 2175-Å feature. The middle panels are same as the left-hand panels, but as a function of the number of clumps in the line of sight contained in the screen for no internal dust (i.e. $\tau_{\rm in}/(\tau_{\rm in} + \tau_{\rm sc}) = 0.0$). The right-hand panels are same as the left-hand panels, but as a function of the number of clumps in the line of sight contained in the screen for $\tau_{\rm in}/(\tau_{\rm in} + \tau_{\rm sc}) = 0.4$. $\chi^2_\nu = 5.1$ results if the Calzetti extinction curve is applied.

panels. The MW extinction curves with and without the 2175-Å feature have larger χ^2_ν than that of the Calzetti extinction curve except for clumpy screens with the average number of clumps of $N = 4$ (see the upper right-hand panel). The overall trends are that small χ^2_ν values (i.e. $\chi^2_\nu < 5.1$) are found in larger N. Uniform dust screens have been explicitly or implicitly assumed in many cases in the literature. These figures indicate that uniform dust screens are good approximations to the real distribution of dust. The two SN extinction curves have χ^2_ν smaller than that of the Calzetti extinction curve for large N.

Fig. 5 gives typical features of parameters as a function of $\tau_{\rm in}/(\tau_{\rm in} + \tau_{\rm sc})$, taking isotropic scattering models as an example. Those parameters are the total optical depth $\tau_{\rm total}(0.3\ \mu{\rm m}) = \tau_{\rm in} + \tau_{\rm sc}$ at 0.3 μm, the metallicity Z, the time after the onset of the first star formation t and the e-folding time-scale $t_{\rm sfr}$. Because the effect of scattering reduces the effective optical depth $\tau_{\rm eff}$ as seen in equations (7)–(9), scattering dust screens require a larger optical depth than no scattering screens; taking models without internal dust, $\tau_{\rm ext}(0.3\ \mu{\rm m}) \sim 5$ for the no scattering screen, $\tau_{\rm ext}(0.3\ \mu{\rm m}) \sim 8$ for the isotropic scattering and $\tau_{\rm ext}(0.3\ \mu{\rm m}) \sim 15$ for the forward-only scattering. The optical depth of the SN 8–40 $M_\odot$ extinction curve requires larger optical depths than those of the other curves. This is because albedo is greater in the SN 8–40 $M_\odot$ curve than the others (see Table 1). Z is smaller on the SN curves than the MW

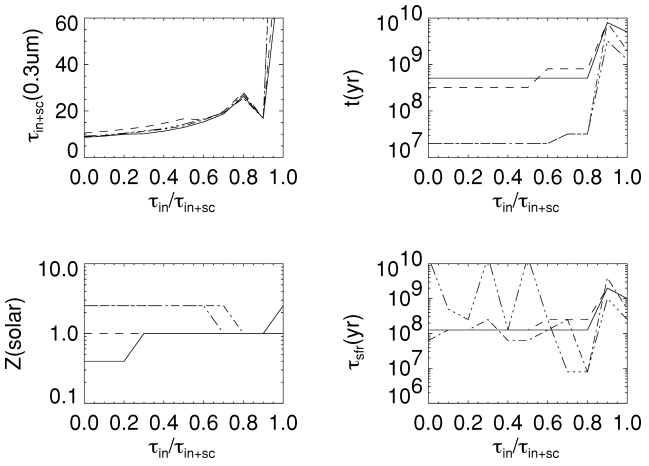

Figure 5. Sample illustration of the total optical depth $\tau_{\rm in} + \tau_{\rm sc}$ at 0.3 μm (upper left), the metallicity Z in units of the solar value (bottom left), the time after the onset of the first star formation t (yr) (upper right) and the e-folding time-scale of the star formation $t_{\rm sfr}$ as a function of the ratio of the optical depth of internal dust to internal+screen dust $\tau_{\rm in}/(\tau_{\rm in} + \tau_{\rm sc})$. The isotropic scattering ($g = 0$) is assumed. Solid lines represent SN dust with 8–30 $M_\odot$, dash lines SN dust with 8–40 $M_\odot$, dash–dot lines MW dust and dash–dot–dot lines pseudo-MW dust without the 2175-Å feature.

curve. On the other hand, t is older on the SN curves than the MW curves. The older t on the SN curves can be attributed to the fact that the slope of the SN curves are flatter than that of the MW curve. To reproduce the redness of the SED, the steep MW curve requires bluer and younger stellar populations.

Fig. 6 shows an example of model SEDs along with the observed SED. It is noted again that the longest wavelength data (i.e. IRAC 8.0 μm) are not used for χ^2_ν fitting. The sample model is obtained by assuming the SN 8–40 $M_\odot$ extinction curve with the isotropic scattering without internal dust. The fitted parameters are $\tau_{\rm sc}(0.3\ \mu{\rm m}) = 10.5$, $t = 3.2 \times 10^8$ yr, $t_{\rm sfr} = 1.3 \times 10^8$ yr and $Z = 1\,Z_\odot$. This model has $\chi^2_\nu = 3.7$ with $\chi^2_{\rm [O\,II]} = 0.4$, $\chi^2_{\rm Ca\,II} = 0.6$ and $\chi^2_{\rm fir} = 2.0$, providing a smaller χ^2_ν than those with the Calzetti extinction curve. Comparing with $\chi^2_\nu = 5.1$, $\chi^2_{\rm [O\,II]} = 0.0$, $\chi^2_{\rm Ca\,II} = 0.3$ and $\chi^2_{\rm fir} = 0.9$ for the best-fitting model with the Calzetti extinction curve, the reduction in χ^2_ν in this SN model is attributed to the reduction in $\chi^2_{\rm SED}$, indicating that the reddening by the SN extinction curve reproduces the SED better than the Calzetti extinction curve.

7 SN II EXTINCTION CURVE

As shown so far, the SN extinction curves synthesized by Hirashita et al. (2005) reasonably reproduce the observed characteristics of ULIRG SST J1604+4303. The goodness of fit is comparable to or better than those with the Calzetti extinction curve. The SN extinction curves must be useful to study young dusty galaxies not only at high redshift but also at modest redshift ($z \sim 1$). We thus present the details of the SN extinction curves from the UV to submillimetre.

Fig. 7 shows $\kappa_{\rm abs}(\lambda)$ of the SN dust along with that of the MW dust, where $\kappa_{\rm abs}(\lambda)$ is the mass absorption cross-section in units of cm^2 g^{-1}. Table 1 gives $\kappa_{\rm ext}(\lambda)$ the mass extinction cross-section, $\kappa_{\rm abs}(\lambda)$ the mass absorption cross-section and albedo for the SN dust; SN 8–30 $M_\odot$ dust in two–four columns and SN 8–40 $M_\odot$ dust in five–seven columns. It is noted that the optical constant of crystalline SiO_2 is used in the models by Hirashita et al. (2005). As a result, the SN curves have spiky features between 9 and 21 μm. The contribution of crystalline SiO_2 to the SN extinction curve is a few per cent at most in the mid- to far-IR range except the spikes at 8.7, 12.25 and 20.5 μm. We smooth the calculated mass extinction coefficient of Si grains around 1 μm to remove small and somehow artificial ripple features arising from large Si grains.

As shown in Fig. 3, the SN extinction curves are flatter than the others: R_V ($=A_V/E_{B-V}$) is 7.8 for the 8–30 $M_\odot$ curve and 5.8 for the 8–40 $M_\odot$, while $R_V = 4.05$ for the Calzetti curve and $R_V = 3.1$ for the MW curve. In other words, for a given amount of reddening, the extinction is greater in the SN curves than the others. As suggested in Fig. 7, the silicate feature around 9.7 μm is much less in the SN dust than in the MW dust. This feature could be used to distinguish the SN extinction curve from the others by means of mid-IR observations in the future.

Another striking feature of the SN curve is the behaviour of $\kappa_{\rm abs}(\lambda)$ from 40 to 1000 μm. Assuming a simple analytic form of $\kappa_{\rm abs}(\lambda) \propto \nu^\beta$, we have $\beta \simeq 1.6$ for the SN dust, while $\beta \simeq 2$ for the MW dust. Single-temperature dust spectral distributions of the form $\nu^\beta B_\nu(T_{\rm dust})$ are widely used to fit observed SED in the far-IR and submillimetre, where $B_\nu(T_{\rm dust})$ is the Planck function. However, fitting only a few data points results in a significant correlation between β and $T_{\rm dust}$ that can account for the data (Blain, Barnard & Chapman 2003): higher $T_{\rm dust}$ with smaller β; $T_{\rm dust}$ derived with the SN dust is 13 per cent higher than that with the MW dust. Assuming the SN dust, we have $T_{\rm dust} = 38.3 \pm 1.4$ K for SST J1604+4304 which is a common characteristics of 104 *IRAS* bright galaxies observed at 850 μm by Dunne et al. (2000), where the best fit was found for $T_{\rm dust} = 35.6 \pm 4.9$ K and $\beta = 1.3 \pm 0.2$.

8 DUST IN SST J1604+4304

Using $T_{\rm dust} = 38.3 \pm 1.4$ K combined with the observed 160 μm flux density and $\kappa_{\rm abs}(80\ \mu{\rm m}) = 22\,{\rm cm^2\,g^{-1}}$ in Table 1 implies that the dust mass $M_{\rm dust}$ in SST J1604+4303 is $2.2 \pm 1.1 \times 10^8\,M_\odot$. Consider a spherical shell with a radius of r and a thickness of δr, and suppose that internal dust fills inside the sphere with r and screen dust in the shell. The mass of the internal dust can be simply approximated to $M_{\rm in} = 4\pi\,(\tau_{\rm in}/\kappa_{\rm ext})r^2/3$ and that of the screen dust to $M_{\rm sc} = 4\pi\,(\tau_{\rm sc}/\kappa_{\rm ext})r^2$, thus $M_{\rm in}/M_{\rm sc} = (\tau_{\rm in}/\tau_{\rm sc})/3$. The best model for the isotropic scattering uniform screen without internal dust has $\tau_{\rm ext}(0.3\ \mu{\rm m}) = 10.5$. In this case, the inferred radius of the spherical shell is about 3.3 kpc or 0.4 arcsec which is comparable to the optical size of SST J1604+4303.

If the star formation history of SST J1604+4303 is described by $t = 3.2 \times 10^8$ yr, $t_{\rm sfr} = 1.3 \times 10^8$ yr and $Z = 1\,Z_\odot$, then the luminosity to mass ratio is 7.6, implying a stellar mass of $2.4 \times 10^{11}\,M_\odot$. During the last 3.2×10^8 yr, $\sim 2.0 \times 10^9$ SNe II exploded in this galaxy. If the dust was mainly supplied by SN explosions, then we have a dust production rate of $\sim 0.1\,M_\odot$ per SN by simply dividing the dust mass by the number of SNe II.

Although χ^2_ν is reduced by adopting the synthesized SN extinction curves, the goodness of fit is far from the perfect fitting (i.e. $\chi^2_\nu \sim 1$). This may come from various reasons. For example, the models for dust formation in SNe II are still coarse and the contribution from the dust formed in AGB stars needs to be included, or the stellar population models are too simple and the real stellar population may be more complex and consist of stars with different ages with different metallicities.

Nozawa et al. (2007) take into account the effect of reverse shock destruction and Hirashita et al. (2008) calculate the extinction curve based on their result. The extinction curves after reverse shock destruction are generally flatter than those of Hirashita et al.

Table 1. Extinction cross-sections of the SN II dust models. A machine-readable version of this table is available as Supporting Information.

	SN 8–30 $M_\odot$			SN 8–40 $M_\odot$		
λ (μm)	κ_{ext} (cm^2 g^{-1})	κ_{abs} (cm^2 g^{-1})	Albedo	κ_{ext} (cm^2 g^{-1})	κ_{abs} (cm^2 g^{-1})	Albedo
6.67e−02	4.69e+04	2.34e+04	5.01e−01	4.86e+04	2.37e+04	5.11e−01
9.12e−02	4.73e+04	2.34e+04	5.05e−01	4.95e+04	2.44e+04	5.07e−01
1.00e−01	4.71e+04	2.30e+04	5.12e−01	4.95e+04	2.44e+04	5.07e−01
1.20e−01	5.07e+04	2.57e+04	4.93e−01	5.23e+04	2.64e+04	4.96e−01
1.40e−01	5.09e+04	2.43e+04	5.23e−01	5.25e+04	2.47e+04	5.29e−01
1.60e−01	4.68e+04	2.03e+04	5.67e−01	4.97e+04	2.12e+04	5.74e−01
1.80e−01	4.04e+04	1.67e+04	5.87e−01	4.54e+04	1.61e+04	6.46e−01
1.90e−01	3.87e+04	1.57e+04	5.94e−01	4.29e+04	1.40e+04	6.74e−01
2.00e−01	3.79e+04	1.50e+04	6.04e−01	4.14e+04	1.23e+04	7.02e−01
2.10e−01	3.77e+04	1.46e+04	6.12e−01	4.04e+04	1.13e+04	7.19e−01
2.20e−01	3.77e+04	1.45e+04	6.15e−01	3.96e+04	1.08e+04	7.26e−01
2.30e−01	3.77e+04	1.46e+04	6.14e−01	3.88e+04	1.07e+04	7.24e−01
2.50e−01	3.75e+04	1.44e+04	6.16e−01	3.72e+04	1.04e+04	7.21e−01
3.00e−01	3.40e+04	1.39e+04	5.92e−01	3.10e+04	9.80e+03	6.84e−01
3.55e−01	3.17e+04	1.32e+04	5.82e−01	2.73e+04	9.00e+03	6.70e−01
3.64e−01	3.14e+04	1.31e+04	5.81e−01	2.68e+04	8.89e+03	6.68e−01
4.41e−01	2.80e+04	1.20e+04	5.71e−01	2.26e+04	8.15e+03	6.40e−01
4.69e−01	2.69e+04	1.16e+04	5.69e−01	2.14e+04	7.84e+03	6.34e−01
5.47e−01	2.48e+04	1.08e+04	5.65e−01	1.93e+04	7.30e+03	6.22e−01
6.17e−01	2.21e+04	9.88e+03	5.53e−01	1.70e+04	6.64e+03	6.10e−01
6.42e−01	2.10e+04	9.66e+03	5.40e−01	1.61e+04	6.51e+03	5.96e−01
6.49e−01	2.08e+04	9.60e+03	5.39e−01	1.60e+04	6.47e+03	5.95e−01
7.00e−01	2.03e+04	9.21e+03	5.46e−01	1.55e+04	6.19e+03	6.00e−01
7.48e−01	1.95e+04	8.90e+03	5.45e−01	1.49e+04	5.98e+03	5.99e−01
8.02e−01	1.86e+04	8.55e+03	5.40e−01	1.41e+04	5.73e+03	5.94e−01
8.66e−01	1.75e+04	8.16e+03	5.34e−01	1.32e+04	5.46e+03	5.86e−01
8.93e−01	1.70e+04	7.99e+03	5.29e−01	1.27e+04	5.36e+03	5.79e−01
9.00e−01	1.68e+04	7.95e+03	5.27e−01	1.26e+04	5.33e+03	5.77e−01
1.00e+00	1.51e+04	7.36e+03	5.12e−01	1.13e+04	4.95e+03	5.62e−01
1.22e+00	1.26e+04	6.08e+03	5.19e−01	9.64e+03	4.12e+03	5.72e−01
1.63e+00	9.48e+03	4.48e+03	5.27e−01	7.52e+03	3.03e+03	5.96e−01
2.19e+00	5.83e+03	3.07e+03	4.74e−01	4.82e+03	2.05e+03	5.75e−01
2.75e+00	4.14e+03	2.42e+03	4.14e−01	3.49e+03	1.62e+03	5.35e−01
3.45e+00	2.73e+03	1.87e+03	3.15e−01	2.40e+03	1.17e+03	5.11e−01
3.80e+00	2.30e+03	1.59e+03	3.06e−01	2.02e+03	9.94e+02	5.08e−01
4.75e+00	1.66e+03	1.13e+03	3.21e−01	1.53e+03	6.87e+02	5.51e−01
6.00e+00	9.46e+02	6.35e+02	3.29e−01	7.70e+02	3.72e+02	5.17e−01
7.00e+00	8.27e+02	5.46e+02	3.40e−01	7.37e+02	3.25e+02	5.58e−01
8.00e+00	6.33e+02	4.72e+02	2.53e−01	4.80e+02	3.10e+02	3.53e−01
8.28e+00	6.21e+02	4.73e+02	2.39e−01	4.70e+02	3.33e+02	2.94e−01
8.71e+00	1.56e+03	1.25e+03	1.97e−01	1.61e+03	1.38e+03	1.46e−01
9.17e+00	6.34e+02	4.99e+02	2.13e−01	5.56e+02	4.62e+02	1.69e−01
9.70e+00	6.63e+02	5.69e+02	1.42e−01	6.42e+02	5.71e+02	1.10e−01
1.13e+01	4.69e+02	3.61e+02	2.29e−01	3.86e+02	3.22e+02	1.64e−01
1.20e+01	3.93e+02	3.25e+02	1.74e−01	3.20e+02	2.79e+02	1.27e−01
1.38e+01	2.56e+02	2.29e+02	1.02e−01	1.94e+02	1.79e+02	8.14e−02
1.53e+01	3.22e+02	2.97e+02	7.65e−02	3.49e+02	3.38e+02	3.37e−02
1.61e+01	6.18e+02	6.01e+02	2.80e−02	8.32e+02	8.23e+02	1.14e−02
1.70e+01	5.95e+02	5.84e+02	1.74e−02	8.06e+02	7.99e+02	8.84e−03
1.79e+01	2.74e+02	2.67e+02	2.68e−02	3.01e+02	2.96e+02	1.61e−02
1.98e+01	2.50e+02	2.45e+02	2.00e−02	2.70e+02	2.67e+02	1.17e−02
2.08e+01	2.90e+02	2.77e+02	4.49e−02	3.08e+02	3.04e+02	1.54e−02
2.19e+01	2.03e+02	1.99e+02	1.97e−02	2.12e+02	2.10e+02	1.07e−02
2.50e+01	1.47e+02	1.45e+02	1.41e−02	1.44e+02	1.43e+02	8.60e−03
4.00e+01	5.69e+01	5.66e+01	4.89e−03	4.55e+01	4.53e+01	3.96e−03
6.00e+01	3.30e+01	3.30e+01	1.61e−03	2.68e+01	2.68e+01	1.34e−03
1.00e+02	1.59e+01	1.59e+01	4.08e−04	1.28e+01	1.28e+01	3.41e−04
1.40e+02	1.09e+01	1.09e+01	1.96e−04	8.45e+00	8.45e+00	1.47e−04
2.00e+02	5.08e+00	5.08e+00	8.02e−05	4.08e+00	4.08e+00	6.63e−05
3.50e+02	2.03e+00	2.03e+00	2.25e−05	1.61e+00	1.61e+00	1.87e−05
8.50e+02	4.38e−01	4.38e−01	3.09e−06	3.57e−01	3.57e−01	2.42e−06
1.00e+03	3.17e−01	3.17e−01	2.00e−06	2.65e−01	2.65e−01	1.61e−06

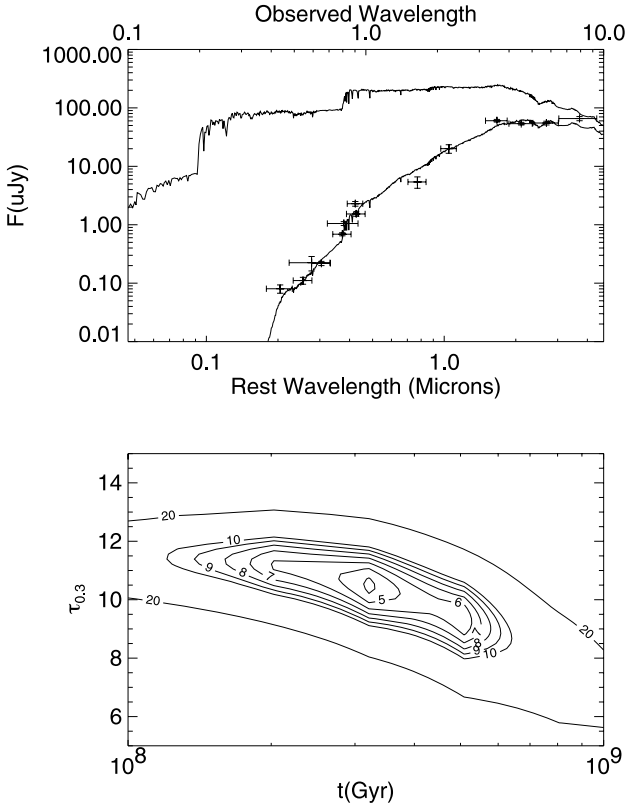

Figure 6. Sample illustration of model SEDs. The illustrated model is obtained by assuming the SN 8–40 $M_\odot$ extinction curve with the isotropic scattering without internal dust. This model has $\chi^2_\nu = 3.7$, $\tau_{sc} = 10.2$ at 0.3 μm, $t = 5.1 \times 10^8$ yr, $t_{sfr} = 2.5 \times 10^8$ yr and $Z = 1\,Z_\odot$. The top panel shows the model spectrum along with the observed SED. The upper curve is the unobscured model spectrum. The bottom panel shows χ^2_ν as a function of t and τ_{sc} at 0.3 μm.

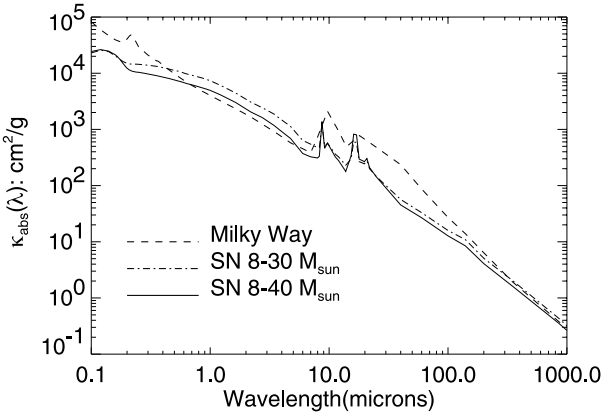

Figure 7. Plot of $\kappa_{abs}(\lambda)$ the absorption cross-section per dust mass in units of cm^2 g^{-1}. Note that spiky features between 9 and 21 μm on the SN curve are mostly attributed to crystal SiO_2 and MgO; spiky features of crystal SiO_2 occur at 8.7, 12.25 and 20.5 μm, while a spike MgO feature at 16.5 μm.

(2005), since small grains are selectively destroyed. In this paper, we simply adopt the extinction curves by Hirashita et al. (2005). In other words, the effect of reverse shock destruction is not taken into account. Indeed, the flat extinction curves after reverse shock destruction are not consistent with the large reddening required for SST J1604+4304. This implies that the reverse shock destruction may not be efficient or that the small grain production by, for example, shattering in warm ISM is occurring (Hirashita et al. 2010), in which case the extinction curve after shattering is similar to that used in this paper. Moreover, the extinction curve by Hirashita et al. (2005) is supported by observations in the sense that it is consistent with the extinction curve derived by Maiolino et al. (2004) for a high-z BAL QSO at $z = 6.2$. Note that the Maiolino et al. (2004)'s extinction curve is also consistent with a high-z ($z = 6.3$) gamma-ray burst (Stratta et al. 2007).

We have shown that a flatter extinction curve (or a larger R_V) than the MW curve fits the SED of SST J1604+4304 better. A flat extinction curve may also be realized if dust growth occurs in dense clouds (Draine 2003). Thus, it is worth investigating whether or not a flat extinction curve predicted from the grain growth fits the observed SED of SST J1604+4304. This is left for future work.

9 CONCLUSIONS

We have applied the SN extinction curves to reproduce the observed properties of SST J1604+4304 which is a young IR galaxy at $z \sim 1$. The SN extinction curves used in this work was obtained from models of unmixed ejecta of SNe II for the Salpeter IMF with a mass range from 8 to 30 $M_\odot$ or 8 to 40 $M_\odot$. These curves are compared with the MW and Calzetti extinction curves. The data used in the χ^2 fitting methods are the fluxes in 13 photometric bands from B to IRAC 5.8 μm, the equivalent width of the [O II]λ3727, the D(Ca II) index and the IR flux in 8–1000 μm.

The effect of dust distributions on the attenuation of starlight was investigated by performing the χ^2 fitting method with various dust distributions. These are the commonly used uniform dust screen, the clumpy dust screen and the internal dust geometry. In addition to these geometries, we have investigated three scattering properties, namely, no scattering, isotropic scattering and forward-only scattering. Judging from the χ^2 values, the uniform screen models with any scattering property provide good approximations to the real dust geometry. Internal dust is inefficient to attenuate starlight and thus cannot be the dominant source of the extinction.

We have found that the SN extinction curves reproduce the data of SST J1604+4304 comparable or better than the Calzetti extinction curve. The MW extinction curve is too steep and is not satisfactory agreement with the data unless several dusty clumps are in the line of sight. This trend may be explained by the abundance of SN-origin dust in these galaxies; SN dust is the most abundant in the young IR galaxy at $z \sim 1$, abundant in local starbursts and less abundant in the Galaxy. If dust in SST J1604+4304 is dominated by SN dust, the dust production rate is $\sim$0.1 $M_\odot$ per SN.

We provide the extinction cross-sections of the SN dust along with albedo from UV to submillimetre wavelengths in Table 1 (see Supporting Information for a machine-readable version of this table).

ACKNOWLEDGMENTS

We thank the anonymous referee for very helpful and constructive comments. This work has been supported in part by Grants-in-Aid for Specially Promoted Research on Innovative Areas (22111503), Specially Promoted Research (20001003) and the Promotion of Science (18104003, 20340038, 22684004) from JSPS. HH is supported by NSC grant 99-2112-M-001-006-MY3.

REFERENCES

Avni Y., 1976, ApJ, 210, 642
Bianchi S., Schneider R., 2007, MNRAS, 378, 973

Blain A. W., Barnard V. E., Chapman S. C., 2003, MNRAS, 338, 733
Borys C. et al., 2006, ApJ, 636, 134
Bruzual G., Charlot S., 2003, MNRAS, 344, 1000
Calzetti D., 2001, PASP, 113, 1449
Calzetti D., Kinney A. L., Storchi-Bergmann T., 1994, ApJ, 429, 582
Carico D. P., Sanders D. B., Soifer B. T., Matthews K., Neugebauer G., 1990, AJ, 100, 70
Chabrier G., 2003, PASP, 115, 763
Code A. D., 1973, in Greenberg J. M., Van de Hulst A. C., eds, Proc. IAU Symp. 52, Interstellar Dust and Related Topics. Reidel, Dordrecht, p. 505
Desai V. et al., 2006, ApJ, 641, 133
Draine B. T., 2003, ARA&A, 41, 241
Dunne L., Eales S., Edmunds M., Ivison R., Alexander P., Clements D. L., 2000, MNRAS, 315, 115
Dunne L., Eales S., Ivison R., Morgan H., Edmunds M., 2003, Nat, 424, 285
Dunne L. et al., 2009, MNRAS, 394, 1307
Dwek E., Galliano F., Jones A. P., 2007, ApJ, 662, 927
Gallerani S. et al., 2010, A&A, 523, 85
Giavalisco M., 2002, ARA&A, 40, 579
Gomez H. L. et al., 2009, MNRAS, 397, 1621
Heger A., Fryer C. L., Woosley S. E., Langer N., Hartmann D. H., 2003, ApJ, 591, 288
Hirashita H., Nozawa T., Kozasa T., Ishii T. T., Takeuchi T. T., 2005, MNRAS, 357, 1077
Hirashita H., Nozawa T., Takeuchi T. T., Kozasa T., 2008, MNRAS, 384, 1725
Hirashita H., Nozawa T., Yan H., Kozasa T., 2010, MNRAS, 404, 1437
Jones A. P., Tielens A. G. G. M., Hollenbach D. J., McKee C. F., 1994, ApJ, 433, 797
Jones A. P., Tielens A. G. G. M., Hollenbach D. J., 1996, ApJ, 469, 740
Kawara K., Nishida M., Phillips M. M., 1989, ApJ, 337, 230
Kawara K. et al., 2010, MNRAS, 402, 335
Kewley L. J., Geller M. J., Jansen R. A., 2004, AJ, 127, 2002
Klaas U., Haas M., Heinrichsen I., Schulz B., 1997, A&A, 325, L21
Kotak R. et al., 2009, ApJ, 704, 306
Kozasa T., Hasegawa H., Nomoto K., 1989, ApJ, 344, 325
Kozasa T., Hasegawa H., Nomoto K., 1991, A&A, 249, 474
Kozasa T., Nozawa T., Tominaga N., Umeda H., Maeda K., Nomoto K., 2009, in Henning Th., Grün E., Steinacker J., eds, ASP Conf. Ser. Vol. 414, Cosmic Dust – Near and Far. Astron. Soc. Pac., San Francisco, p. 43
Maiolino R., Schneider R., Oliva E., Bianchi S., Ferrara A., Mannucci F., Pedani M., Roca Sogorb M., 2004, Nat, 431, 533
Maiolino R. et al., 2006, Mem. Soc. Astron. Ital., 77, 643
Morgan H. L., Edmunds M. G., 2003, MNRAS, 343, 427
Natta A., Panagia N., 1984, ApJ, 287, 228
Noll S. et al., 2009, A&A, 499, 69
Nozawa T., Kozasa T., Umeda H., Maeda K., Nomoto K., 2003, ApJ, 598, 785
Nozawa T., Kozasa T., Habe A., 2006, ApJ, 648, 435
Nozawa T., Kozasa T., Habe A., Dwek E., Umeda H., Tominaga N., Maeda K., Nomoto K., 2007, ApJ, 666, 955
Nozawa T. et al., 2008, ApJ, 684, 1343
Nozawa T., Kozasa T., Tominaga T., Maeda K., Umeda H., Nomoto K., Krause O., 2010, ApJ, 713, 356
Puxley P. J., Brand P. W. J. L., 1994, MNRAS, 266, 431
Rho J. et al., 2008, ApJ, 673, 271
Rigopoulou D., Lawrence A., Rowan-Robinson M., 1996, MNRAS, 278, 1049
Salpeter E. E., 1955, ApJ, 121, 161
Schneider R., Ferrara A., Salvaterra R., 2004, MNRAS, 351, 1379
Stratta G., Maiolino R., Fiore F., D'Elia V., 2007, ApJ, 661, L9
Temim T., Slane P., Reynolds S. P., Raymond J. C., Borkowski K. J., 2010, ApJ, 710, 309
Todini P., Ferrara A., 2001, MNRAS, 325, 726
Valiante R., Schneider R., Bianchi S., Andersen A. C., 2009, MNRAS, 397, 1661
Zafar T., Watson D. J., Malesani D., Vreeswijk P. M., Fynbo J. P. U., Hjorth J., Levan A. J., Michałowski M. J., 2010, A&A, 515, 94

APPENDIX A: TWO STREAM APPROXIMATION FOR RADIATION TRANSFER IN A DUSTY SLAB

The two stream approximation in radiation transfer was applied to an spherically symmetric dust envelope surrounding a star by Code (1973). Here we consider a plane-parallel dust slab.

We measure distance z outward for a plane-parallel slab, then

$$\frac{\mu}{\rho}\frac{\mathrm{d}I_\nu(z,\mu)}{\mathrm{d}z} = j_\nu - \kappa_\nu I_\nu(z,\mu) + \frac{\sigma_\nu}{4\pi}\int_{4\pi} p(\mu,\mu')I_\nu(z,\mu)\,\mathrm{d}\omega', \tag{A1}$$

where $I_\nu(z,\mu)$ is the specific intensity, $\mu = \cos\theta$ the directional cosine, ν the frequency, κ_ν the mass extinction coefficient, σ_ν the mass scattering coefficient, ρ the mass density of dust and j_ν the ratio of the stellar emission per unit dust mass. The phase function $p(\mu,\mu')$ is defined by

$$\int_{4\pi} p(\mu,\mu')\,\mathrm{d}\omega' = 4\pi \quad \text{or} \quad \frac{1}{2}\int_{-1}^{1} p(\mu,\mu')\,\mathrm{d}\mu' = 1. \tag{A2}$$

By introducing the optical depth τ_ν which is defined by $\mathrm{d}\tau_\nu = -\rho\kappa_\nu \mathrm{d}z$, the radiation transfer equation is reduced to

$$\mu\frac{\mathrm{d}I_\nu(\tau,\nu)}{\mathrm{d}\tau_\nu} = -j_\nu/\kappa_\nu + I_\nu - \frac{\gamma_\nu}{2}\int_{-1}^{1} p(\mu,\mu')I_\nu(\tau,\mu')\,\mathrm{d}\mu', \tag{A3}$$

where $\gamma_\nu = \sigma_\nu/\kappa_\nu$ is the albedo. In what follows, we omit the subscript ν for simplicity.

A1 Slab illuminated at the backside

Consider a slab which contains no emitters and illuminated at the backside, i.e. $j_\nu = 0$. In the two stream approximation, the specific intensity $I(\tau,\mu)$ is represented by the specific intensities at two specified directions at $\pm\mu$; $I^+(\tau) = I(\tau,\mu)$ and $I^-(\tau) = I(\tau,-\mu)$ for $0 \le \mu \le 1$. $I^+(\tau)$ and $I^-(\tau)$ are assumed to be independent of μ over the upward and the downward hemispheres, respectively.

According to Code (1973), we introduce the forward and backward scattering coefficients σ^+ and σ^- which are defined by

$$\frac{\sigma^+}{\sigma} = \frac{1}{2}\int_0^1 p(\mu,\mu')\,\mathrm{d}\mu' \quad \text{and} \quad \frac{\sigma^-}{\sigma} = \frac{1}{2}\int_0^1 p(\mu,-\mu')\,\mathrm{d}\mu', \tag{A4}$$

respectively. Note that $\sigma^+ + \sigma^- = \sigma$. A modified asymmetry factor g is defined by

$$g = \frac{\sigma^+ - \sigma^-}{\sigma}, \tag{A5}$$

note that $g = 1$ for forward scattering, $g = -1$ for backward scattering and $g = 0$ for isotropic scattering. Then using the relations $\sigma^+/\sigma = (1+g)/2$ and $\sigma^-/\sigma = (1-g)/2$, the equations (A3) is reduced to

$$\mu\frac{\mathrm{d}I^+(\tau)}{\mathrm{d}\tau} = I^+(\tau) - \gamma\frac{(1+g)}{2}I^+(\tau) - \gamma\frac{(1-g)}{2}I^-(\tau), \tag{A6}$$

$$-\mu\frac{\mathrm{d}I^-(\tau)}{\mathrm{d}\tau} = I^-(\tau) - \gamma\frac{(1+g)}{2}I^-(\tau) - \gamma\frac{(1-g)}{2}I^+(\tau). \tag{A7}$$

Here we replace the optical depth along the z-axis with the optical depth along the line of sight $\mathrm{d}\tau_{\mathrm{ext}} = \mathrm{d}\tau/\mu$ and introduce new

variables $x = I^+ - I^-$ and $y = I^+ + I^-$, the above equations become simply

$$\frac{\mathrm{d}x}{\mathrm{d}\tau_{\rm ext}} = (1-\gamma)\,y \quad \text{and} \quad \frac{\mathrm{d}y}{\mathrm{d}\tau_{\rm ext}} = (1-\gamma g)\,x. \tag{A8}$$

Then the solutions of $I^+(\tau_{\rm ext})$ and $I^-(\tau_{\rm ext})$ are given by

$$I^+(\tau_{\rm ext}) = \frac{1}{2}[(\beta+1)A\,\exp(\alpha\tau_{\rm ext}) - (\beta-1)B\,\exp(-\alpha\tau_{\rm ext})], \tag{A9}$$

$$I^-(\tau_{\rm ext}) = \frac{1}{2}[(\beta-1)A\,\exp(\alpha\tau_{\rm ext}) - (\beta+1)B\,\exp(-\alpha\tau_{\rm ext})], \tag{A10}$$

where $\alpha^2 = (1-\gamma)(1-\gamma g)$ and $\beta = [(1-\gamma g)/(1-\gamma)]^{1/2}$. Using the boundary conditions of $I^-(0) = 0$ and $I^+(\tau_{\rm 1ext}) = I_0$ for determining the constants A and B, where $\tau_{\rm 1ext}$ is the optical depth of the slab along the line of sight, then the emergent intensity $I^+(0)$ is given by

$$I^+(0) = \frac{2\beta I_0}{(\beta+1)\exp(\alpha\tau_{\rm 1ext}) + (\beta-1)\exp(-\alpha\tau_{\rm 1ext})}. \tag{A11}$$

A2 Slab containing emitters

We now consider a slab that contains emitters, i.e. stars. The slab is illuminated by these internal stars only. Then the radiation transfer equations for $I^{\pm}$ are simply given by

$$\mu\frac{\mathrm{d}I^+(\tau)}{\mathrm{d}\tau} = I^+(\tau) - \gamma\frac{(1+g)}{2}I^+(\tau) - \gamma\frac{(1-g)}{2}I^-(\tau) - \Lambda, \tag{A12}$$

$$-\mu\frac{\mathrm{d}I^-(\tau)}{\mathrm{d}\tau} = I^-(\tau) - \gamma\frac{(1+g)}{2}I^-(\tau) - \gamma\frac{(1-g)}{2}I^+(\tau) - \Lambda, \tag{A13}$$

where $\Lambda = j_\nu/\kappa_\nu$. Then $x = I^+ - I^-$ and $y = I^+ + I^-$ can be determined by solving the following simultaneous equations:

$$\frac{\mathrm{d}x}{\mathrm{d}\tau_{\rm ext}} = (1-\gamma)\,y - 2\Lambda \quad \text{and} \quad \frac{\mathrm{d}y}{\mathrm{d}\tau_{\rm ext}} = (1-\gamma g)\,x. \tag{A14}$$

The intensities $I^{\pm}(\tau_{\rm ext})$ are given by

$$I^+(\tau_{\rm ext}) = \frac{1}{2}(\beta+1)\,[A - E_0(\tau_{\rm ext})]\exp(\alpha\tau_{\rm ext}) - \frac{1}{2}(\beta-1)\,[B - E_1(\tau_{\rm ext})]\exp(-\alpha\tau_{\rm ext}), \tag{A15}$$

$$I^-(\tau_{\rm ext}) = \frac{1}{2}(\beta-1)\,[A - E_0(\tau_{\rm ext})]\exp(\alpha\tau_{\rm ext}) - \frac{1}{2}(\beta+1)\,[B - E_1(\tau_{\rm ext})]\exp(-\alpha\tau_{\rm ext}), \tag{A16}$$

where

$$E_0(\tau_{\rm ext}) = \int_0^{\tau_{\rm ext}} \Lambda(\tau'_{\rm ext})\exp\left(-\alpha\tau'_{\rm ext}\right)\mathrm{d}\tau'_{\rm ext} \qquad \text{and}$$

$$E_1(\tau_{\rm ext}) = \int_0^{\tau_{\rm ext}} \Lambda(\tau'_{\rm ext})\exp\left(\alpha\tau'_{\rm ext}\right)\mathrm{d}\tau'_{\rm ext}. \tag{A17}$$

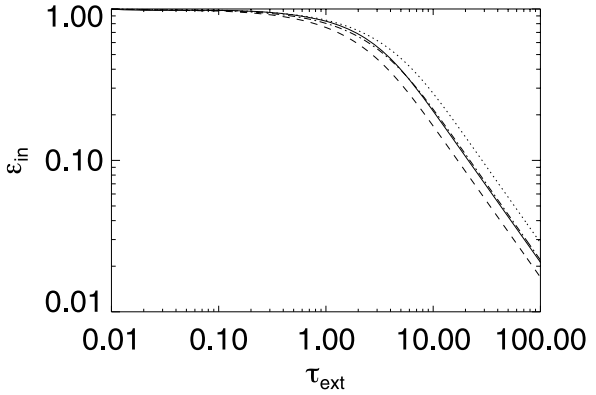

Figure A1. Plot of the apparent extinction $\epsilon_{\rm in}$ as a function of the optical depth along the line of sight $\tau_{\rm ext}$. The geometry is the internal dust with $\gamma = 0.65$ and $g = 0$ (spherical scattering). The solid line represents the solution of equation (A19) for $\Lambda =$ const against $\tau_{\rm ext}$. The other lines represent the absorption approximated by $\epsilon_{\rm in} = (1-\mathrm{e}^{-\tau_{\rm eff}})/\tau_{\rm eff}$; the dotted line for $\tau_{\rm eff} = (1-\gamma)\tau_{\rm ext}$, the dashed line for $\tau_{\rm eff} = (1-\gamma)^{0.5}\tau_{\rm ext}$ and the dash–dot line for $\tau_{\rm eff} = (1-\gamma)^{0.75}\tau_{\rm ext}$.

Given the boundary conditions of $I^-(0) = I^+(\tau_{\rm 1ext}) = 0$, the emergent intensity $I^+(0)$ is given by

$$I^+(0) = 2\beta\frac{(\beta+1)E_0(\tau_{\rm 1ext})\exp(\alpha\tau_{\rm 1ext}) - (\beta-1)E_1(\tau_{\rm 1ext})\exp(-\alpha\tau_{\rm 1ext})}{(\beta+1)^2\exp(\alpha\tau_{\rm 1ext}) - (\beta-1)^2\exp(-\alpha\tau_{\rm 1ext})}. \tag{A18}$$

If $\Lambda =$ const against $\tau_{\rm ext}$, $I^+(0) \to \Lambda\tau_{\rm 1eff}$ for $\tau_{\rm 1ext} \to 0$. Thus, the apparent extinction $\epsilon_{\rm in}$ as defined in equation (1) is

$$\epsilon_{\rm in} = \frac{2\beta}{\alpha\tau_{\rm 1ext}}\frac{(\beta+1)[\exp(\alpha\tau_{\rm 1ext}) - 1] - (\beta-1)[1 - \exp(-\alpha\tau_{\rm 1ext})]}{(\beta+1)^2\exp(\alpha\tau_{\rm 1ext}) - (\beta-1)^2\exp(-\alpha\tau_{\rm 1ext})}. \tag{A19}$$

Fig. A1 compares equation (A19) with the approximations by $\epsilon_{\rm in} = (1-\mathrm{e}^{-\tau_{\rm eff}})/\tau_{\rm eff}$ for $\tau_{\rm eff} = (1-\gamma)\tau_{\rm ext}$, $\tau_{\rm eff} = (1-\gamma)^{0.5}\tau_{\rm ext}$ and $\tau_{\rm eff} = (1-\gamma)^{0.75}\tau_{\rm ext}$. The geometry is internal dust with $\gamma = 0.65$ and $g = 0$. As shown in Fig. A1, $\tau_{\rm eff} = (1-\gamma)^{0.75}\tau_{\rm ext}$ approximates to equation (A19) better than $\tau_{\rm eff} = (1-\gamma)^{0.5}\tau_{\rm ext}$ for the isotropic scattering.

SUPPORTING INFORMATION

Additional Supporting Information may be found in the online version of this article:

Table 1. Extinction cross-sections of the SN II dust models.

Please note: Wiley-Blackwell are not responsible for the content or functionality of any supporting materials supplied by the authors. Any queries (other than missing material) should be directed to the corresponding author for the article.

This paper has been typeset from a TEX/LATEX file prepared by the author.